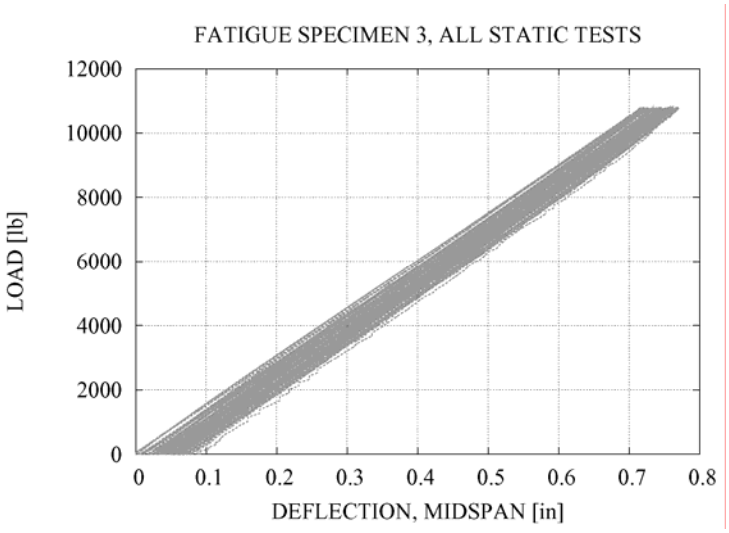

Figure 3.25: Load vs. Deflection for All Static Loadings (Fatigue Specimen 3)

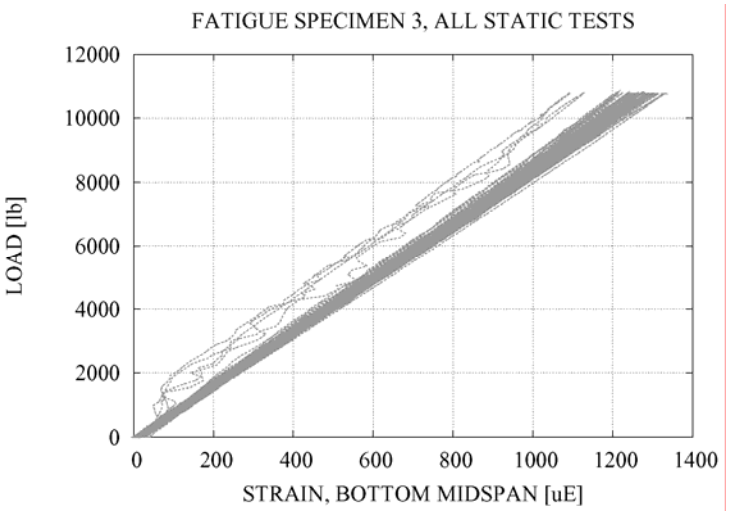

Figure 3.26: Load vs. Strain for All Static Loadings (Fatigue Specimen 3)

3.7 Summary

The results for all of the flexural test specimens are summarized in Table 3.6 for convenience. Note that Table 2.2 contains information about the specimens' geometry and test setups.

Table 3.6: Summary of Test Results for All Flexural Test Specimens

Specimen	span [ft-in]	F_{ult} [lb]	D_{ult} [in]	ε_{ult} [$\mu\varepsilon$]	w [lb]	Remarks
A6	8'	20,950	2.48	9,072	67	
A12	8'	44,310	3.03	10,221	127	
A18	8'	48,880	2.49	—	191	
A24	8'	36,190	1.21	4,142	249	
A30	8'	100,810	2.61	8,500 (estimated)	312	
A6 Repaired	8'	33,890	3.27	12,900	105	
A18 Repaired	8'	89,580	2.60	10,443 (extrapolated)	299	
A24 Repaired	8'	75,260	1.61	6,187	371	
A30 Repaired	8'	86,956	1.58	6,737	453	
Fatigue Baseline	12'	45,160	3.20	5,656	341	
Fatigue Specimen 1	12'	—	—	—	—	not tested to failure
Fatigue Specimen 2	12'	—	—	—	—	not tested
Fatigue Specimen 3	12'	—	—	—	—	not tested to failure
32ft Damaged	31'	40,000	2.75	—	—	
32ft Clarkson	31'	75,000	—	—	—	
32ft Repaired	31'	125,000	7.56	8,347	—	
Steel 2 Rebars	8'	35,280	2.33	8,723	187	
Steel 4 Rebars	8'	39,290	2.76	9,356	193	

F_{ult}: ultimate total load (sum of 2 applied loads for 4-point bending)
D_{ult}: ultimate midspan deflection
ε_{ult}: ultimate bottom midspan strain
w: weight of the specimen
span: span between supports

—: data were not measured or were unavailable

Chapter 4

Analytical Calculation and Models

This chapter focuses on the development of simplified expressions for shear and flexural stiffness' in the longitudinal direction that can be used to predict deflections within a reasonable accuracy. It also highlights the efforts to assess the failure criterion for the decks. Finally, the development of FE models and modeling of stress distribution at the critical core-face interface based on the FE models are discussed.

4.1 Prediction of Shear and Flexural Stiffness from Material Properties

The objective of this section is to determine a simple analytical expression to estimate the flexural (*EI*) and shear (*GA*) stiffness of the FRPH panels in the longitudinal direction. This expression would provide the design engineer with a tool to quickly predict the overall panel response in lieu of running a detailed FE analysis, which often requires considerable computational effort and resources. The sought after expression would serve as a simple prediction of member's stiffness without implementing all of the details about the material properties at the lowest level and internal geometric panel structure as done by Davalos et al. [Davalos et al. 2001][16], refer to Sec. 2.4.

The formula is based on the following assumptions:

1. The material properties for the flat, flute, and face laminates are known from coupon testing. Young's modulus was determined for all laminates, shear modulus only for ChopSM which has essentially isotropic properties. Then $G = E/(2+2\nu)$.

[16] Reader is encouraged to refer to [Davalos et al. 2001] to acquire basic idea about approach of Davalos et al. Their resulting formulas are based on numerous assumptions and extensive notation which prevented those formulas from being cited here, because proper preliminaries would also need to be established. Reader can get more complete picture by directly referring to [Davalos et al. 2001].

2. The cross-section of the deck can be idealized as the cross-section of an I-Beam. Since FRPH panels consist of several different materials (e.g. ChopSM in the core, unidirectional mat in the faces), it is convenient to transform the section dimensions so that the section can be treated as thought it were composed from one material only. ChopSM was chosen as the base material for all transformed sections. Then, the flanges of the I-Beam correspond to the faces of the FRPH deck, while the web of I-Beam represents the core of FRPH deck (having a thickness equal to the sum of all flat and flute thicknesses in the core). For wrapped beams, the area of the wrap and re-bonding layers is also included in this idealized I-Beam. Similarly, for the panels with internal steel reinforcement, the steel reinforced beams, steel is also accounted for.
3. Contribution of both core and face laminates is included in the flexural stiffness (*EI*). Nevertheless, only the core is accounted for when expressing the shear stiffness (*GA*). This is due to the fact, that shear deformation of faces is negligible.

Based on the above assumptions, the following two formulas are suggested:

$$EI = \sum_{i=1}^{n} E_i G_i = E_{base} \sum_{i=1}^{n} I_{transf,i} \qquad \text{(Eqn. 4.1)}$$

$$GA = \sum_{i=1}^{m} G_i A_i = G_{base} \sum_{i=1}^{m} A_{transf,i} \qquad \text{(Eqn. 4.2)}$$

Where E_{base} and G_{base} are Young's and shear moduli of the ChopSM (core material), the base material into which the section is transformed; n is the total number of all subsections, m is number of core subsections; $I_{transf;i}$ is the moment of inertia of the ith subsection about the neutral axis of the whole section (the summation is made over the whole section), while $A_{transf;i}$ is the area of the core i^{th} subsection (in this case the summation is made only over the core subsections).

4.1.1 Sample Calculation of EI and GA (for Specimen A24 Repaired)

EI and GA were calculated for each specimen using a spreadsheet. Figure 4.1 and Table 4.1 illustrate the typical procedure. The first step was to decompose the section into rectangular subsections in order to simplify subsequent calculations (see Figure 4.1 for the sketch of this division). Individual subsections were then transformed into the core material.

The dimensions of the transformed subsections and distance of their center of gravity from the top of the whole section are inputs for Table 4.1 which is used to calculate I_{transf} and A_{core}. The procedure is straightforward and is based on the following routine calculations (refer to legend to Table 4.1):

1. Center of gravity for the whole section is calculated as:

$$C_g = \frac{\sum Ay_c}{\sum A}$$

2. Then, the moment of inertia of the whole section is equal to the sum of the contribution of the individual subsections (each subsection contributes by the moment of inertia about its own axis and by Steiner's supplement):

$$I_{transf} = \sum_i I_i + \sum_i (y_i - y_c)^2 A_i$$

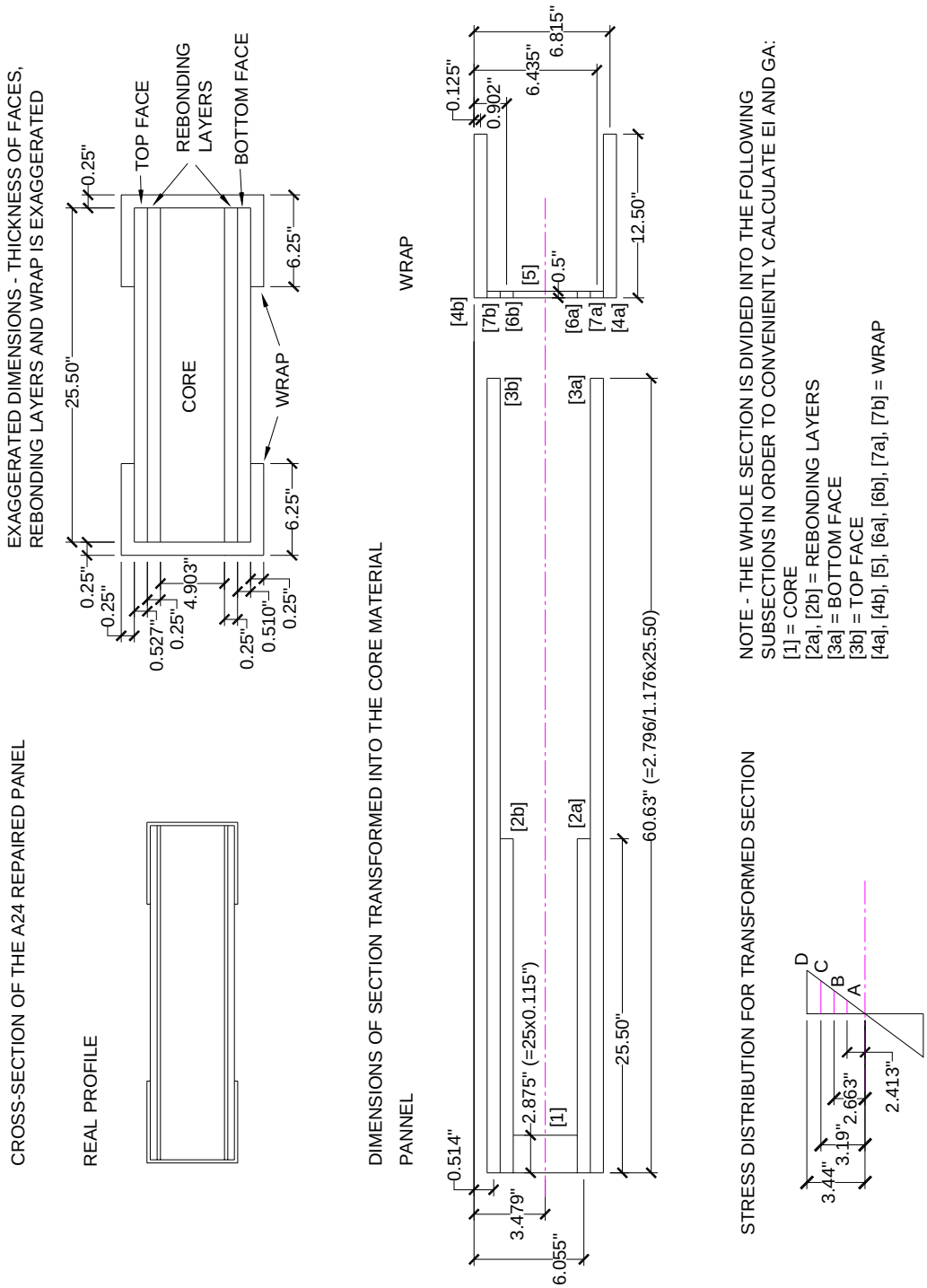

Figure 4.1: Sketch of Cross-Section of Specimen A24 Repaired

Table 4.1: Calculation of Sectional Properties for Specimen A24 Repaired (Refer to Figure 4.1)

Id	w [in]	h [in]	n	w_{transf} [in]	y_c [in]	A [in^2]	$A\,y_c$ [in^3]	I_{own} [in^4]	I_{suppl} [in^4]	I_{tot} [in^4]
1	2.875	4.903	1.000	2.88	3.48	14.10	49.04	28.24	0.02	28.26
2a	25.500	0.250	1.000	25.50	6.06	6.38	38.60	0.03	43.44	43.48
2b	25.500	0.250	1.000	25.50	0.90	6.38	5.75	0.03	41.21	41.24
3a	25.500	0.510	2.378	60.63	6.44	30.92	198.97	0.67	276.53	277.20
3b	25.500	0.527	2.378	60.63	0.51	31.95	16.42	0.74	274.38	275.12
4a	12.500	0.250	1.000	12.50	6.82	3.13	21.30	0.02	35.50	35.52
4b	12.500	0.250	1.000	12.50	0.13	3.13	0.39	0.02	34.43	34.45
5	0.500	4.903	1.000	0.50	3.48	2.45	8.53	4.91	0.00	4.91
6a	0.500	0.250	1.000	0.50	6.06	0.13	0.76	0.00	0.85	0.85
6b	0.500	0.250	1.000	0.50	0.90	0.13	0.11	0.00	0.81	0.81
7a	0.500	0.510	1.000	0.50	6.44	0.26	1.64	0.01	2.28	2.29
7b	0.500	0.527	1.000	0.50	0.51	0.26	0.14	0.01	2.26	2.27

Properties for Whole Transformed Section:

A_{core} = 16.55 in^2

A = 99.19 in^2

Ay_c = 341.65 in^2

C_g = 3.44 in

I_{total} = 746.39 in^4

LEGEND:

Id: subsection designation

w: width of subsection in "real material"

h: height of subsection

n: modular ratio = $E_{material}/E_{core}$

w_{transf}: width of subsection in "transformed material" (ChopSM)

y_c: distance from subsection's center of gravity to the top of section

A: area of subsection

I_{own}: moment of inertia about subsection's axis

I_{suppl}: Steiner's supplement to moment of inertia

I_{tot}: $I_{tot} = I_{own} + I_{supp}$

C_g: distance from center of gravity to the top of section

4.1.2 Sectional Properties and Stiffness for All Tested Specimens

Using the procedure described in detail in Section 4.1.1, the cross-section properties were calculated for all test specimens, and a summary is provided in Table 4.4.

4.1.3 Comparison of Theoretical and Experimental Deflections

When comparing theoretical deflections based on the calculated values for *EI* and *GA* to experimental data, the points of correlation were the deflections corresponding to a load

approximately equal to the maximum load (or the maximum load in linear range). Theoretical deflections due to flexure and shear were calculated for the same corresponding load. This comparison is summarized in Figure 4.2, which shows that this simple estimate lies within 20% of the experimental values for all specimens tested, except for the *Steel Reinforced* (*With Two Rebars*) specimen. The discrepancy for specimen *Steel Reinforced* (*With Two Rebars*) is attributed to scatter in material properties.

Table 4.2: Summary of Sectional Properties for All Tested Specimens

Specimen	I_{transf} [in^4]	A_{core} [in^2]	EI [10^6xlbxin^2]	GA [10^6xlb]	Q [in^3]
A6	132	3.4	155.2	1.5	23.02
A12	257	6.8	302.2	3.0	45.20
A18	389	10.1	457.5	4.5	68.16
A24	490	13.5	576.2	6.0	85.52
A30	666	15.2	783.2	6.8	118.20
A6 Repaired	234	6.5	275.2	2.9	37.00
A18 Repaired	604	12.7	710.3	5.7	98.80
A24 Repaired	746	16.6	877.3	7.4	121.14
A30 Repaired	974	18.1	1,145.4	8.1	154.06
Fatigue Baseline	700	12.6	823.2	5.6	84.18
Fatigue Specimen 1	700	12.6	823.2	5.6	84.18
Fatigue Specimen 2	700	12.6	823.2	5.6	84.18
Fatigue Specimen 3	700	12.6	823.2	5.6	84.18
32ft Damaged	10,118	42.1	11,898.8	18.9	221.11
32ft Clarkson	10,389	45.6	12,217.5	20.4	221.11
32ft Repaired	11,617	45.6	13,661.6	20.4	269.29
Steel 2 Rebars	206	7.8	242.3	3.5	53.40
Steel 4 Rebars	238	7.8	279.9	3.5	54.50

I_{transf}: moment of inertia of section transformed into the core (ChopSM) material
A_{core}: area of sandwich core
EI: flexural stiffness
GA: shear stiffness
Q: static moment of cross-section portion above the failure plane

4.1.4 Alternate Approach to Determine Flexural and Shear Panel Stiffness

Another approach for determination of flexural and shear panel stiffness' was also used. The total deflection of a beam at a certain point is composed of deflections due to flexural and

shear deformations. If deflection is measured experimentally, one equation for two unknowns (*EI* and *GA*) is obtained. A second equation for the same two unknowns can be obtained if the experimental deflection is measured in two different test setups for the same panel (e.g. the panel is supported on different span lengths).

The disadvantage of this method is that the whole panel must be tested, preferably in two different test setups (the reason for this is provided later). This experimental determination of *EI* and *GA* stiffness is obviously more accurate (providing that correct test setups are chosen) than the simplified method described earlier. However, proof-testing is not feasible for most design situations.

Derivation of Formulas for Deflections Due to Bending and Shear

All of the following formulas were derived using the principle of virtual work[17] and verified (deflections caused by moment only) by "ready to use formulas" from [Hibbeler 1995]. The shear correction factor, κ, was considered to be 1:0.

[17] Based on following fundamental equation:

$$\delta = \int \frac{M\overline{M}}{EI} dx + \int \frac{Q\overline{Q}}{\kappa GA} dx \qquad \text{(Eqn. 4.3)}$$

where *EI* and *GA* are flexural and shear stiffness, respectively. *Q* and *M* are internal shear force and moment resulting from the actual load, and $\overline{Q}$ and $\overline{M}$ are the virtual forces induced by a virtual unit load at the point of unknown deflection.

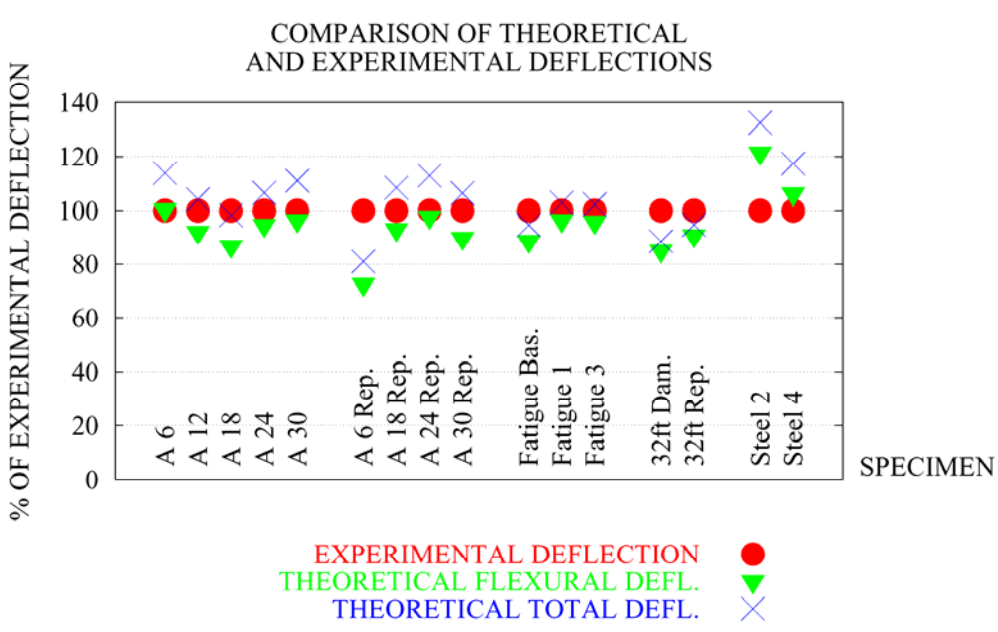

Figure 4.2: Comparison of Theoretical and Experimental Deflections

3-point Bending:

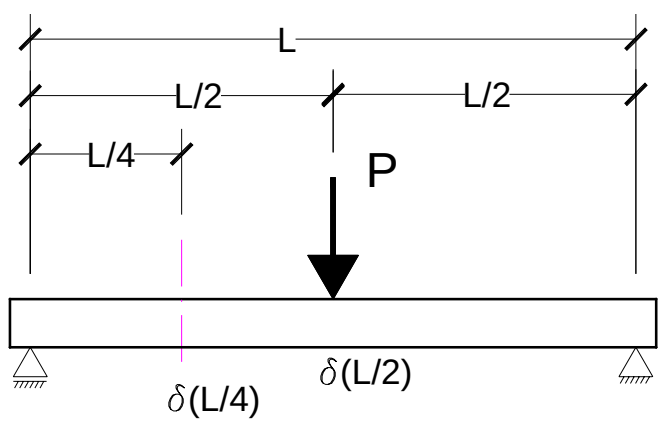

Figure 4.3: 3-point Bending Test

$$\delta_{total}(L/2) = \delta_{bending} + \delta_{shear} = \frac{PL^3}{48EI} + \frac{PL}{4GA} \qquad \text{(Eqn. 4.4)}$$

$$\delta_{total}(L/4) = \delta_{bending} + \delta_{shear} = \frac{11PL^3}{768EI} + \frac{PL}{8GA} \qquad \text{(Eqn. 4.5)}$$

4-point bending:

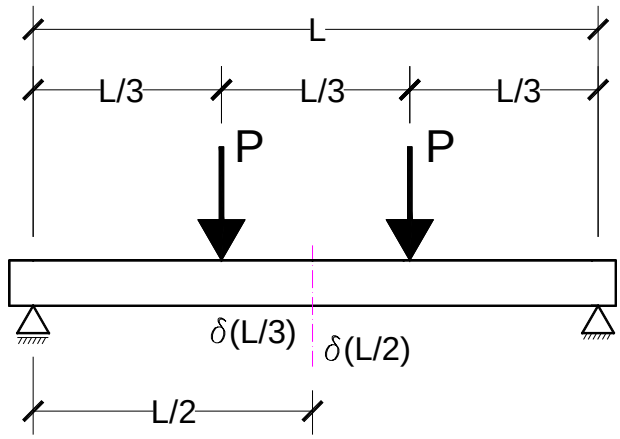

Figure 4.4: 4-point Bending Test

$$\delta_{total}(L/3) = \delta_{bending} + \delta_{shear} = \frac{5PL^3}{162EI} + \frac{PL}{3GA} \qquad \text{(Eqn. 4.6)}$$

$$\delta_{total}(L/2) = \delta_{bending} + \delta_{shear} = \frac{23PL^3}{648EI} + \frac{PL}{3GA} \qquad \text{(Eqn. 4.7)}$$

As one could expect (and is apparent from comparison of Equations 4.6 and 4.7), the difference in deflection between the deflection at the loading point and midspan is due to the bending moment only, since there is no shear in the constant moment region between the loading points. If we isolate the part of the beam between the loading points having length *L/3* and apply end moments *PL/3*, then the additional deflection (to the deflection at the loading point) at the midspan caused solely by the moment is:

$$\delta_{increase} = \delta_{L/2} - \delta_{L/3} = \frac{PL^3}{216EI}$$

Application to Selected Tests

Solving Equations 4.4 and 4.5 for two unknowns *EI* and *GA* yields:

$$GA = \frac{3PL}{4\left(11\delta_{(L/2)} - 16\delta_{(L/4)}\right)}$$

$$EI = \frac{PL^3}{128\left(2\delta_{(L/4)} - \delta_{(L/2)}\right)}$$

The above derived formulas were used to calculate the experimental values of *EI* and *GA* for each specimen of *Series A* (except for *A18*, for which only the mid-span deflection was recorded). In addition, the procedure described in Section 0 was also used to calculate the theoretical values of *EI* and *GA*.

Table 4.3 shows that *EI* and *GA* based solely on experimental values of deflection do not show any clear trend (especially *GA*) and even do not compare well to theoretical values.

Table 4.3: Comparison of Theoretical and Experimental EI and GA for Series A

Specimen	Theoretical		Experimental	
	EI [10^6xlbxin^2]	GA [10^6xlb]	EI [10^6xlbxin^2]	GA [10^6xlb]
A6	155.2	1.5	140.4	-1.8
A12	302.2	3.0	329.2	2.1
A18	457.5	4.5	n.a.	n.a.
A24	576.2	6.0	873.4	1.9
A30	738.2	6.8	892.6	5.6

The reason for this may be that the measurement precision required to accurately determine *EI* and *GA* from deflection readings at two different points in a beam subjected to 3-point bending may have exceeded the capabilities of our test setup. A less sensitive setup for

obtaining *EI* and *GA* would be where the deflection at one point is caused primarily by shear deformation, while the other deflection reading is caused mainly by flexural deformation.

The same procedure was conducted for the *Fatigue Baseline* specimen (loaded in 4-point bending) by solving Equations 4.6 and 4.7 for *EI* and *GA*:

$$GA = \frac{PL}{23\delta_{(L/3)} - 20\delta_{(L/2)}}$$

$$EI = \frac{PL^3}{216\left(\delta_{(L/2)} - \delta_{(L/3)}\right)}$$

The results for the *Fatigue Baseline* specimen are summarized on Table 4.4. The better comparison of theoretical and experimental values is most likely due to the fact that the difference between deflections is caused solely due to the flexural deformation (between the loading point and midspan).

Table 4.4: Comparison of Theoretical and Experimental EI and GA for Fatigue Baseline Specimen

Specimen	Theoretical		Experimental	
	EI [10^6xlbxin^2]	GA [10^6xlb]	EI [10^6xlbxin^2]	GA [10^6xlb]
Fatigue Baseline	823.2	5.6	817.6	4.1

4.2 Search for Failure Criterion

Since all of the flexural specimens failed by horizontal shear at the interface between the core and face laminates[18] (see Figure 4.5), the authors tried to establish a criteria to analytically predict the ultimate load carrying capacity of the specimens based on an ultimate shear stress at the interface.

[18] For wrapped specimens this resulted also in wrap rupture (Figure 4.5(b)) or delamination (Figure 4.5(c)).

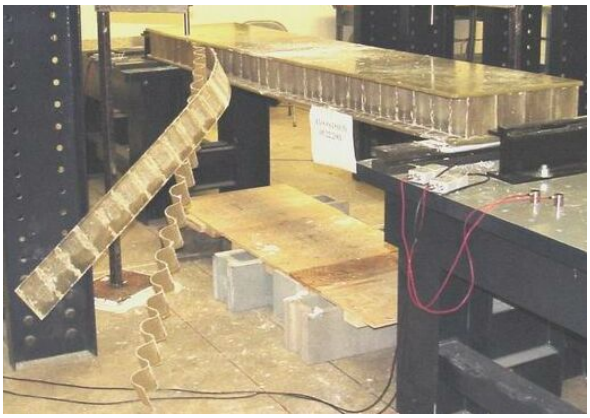

(a) Specimen A18

(b) 32-ft-long Repaired Beam

(c) Specimen A18 Repaired (Horizontal Shear Failure Resulted in Wrap Delamination)

Figure 4.5: Photographs of Horizontal Shear Failure for Different Specimens

These calculations were based on the following assumptions:

1. The material properties for the flat, flute, and face laminates (especially Young's modulus) are known from coupon testing.
2. The cross-section of the deck can be idealized as an I-Beam, whose dimensions are all transformed into core material (see Sec. 4.1.1 for details on calculating the section properties).
3. Longitudinal strains are linear through the depth of the panel.
4. The bottom and top panel faces are perfectly bonded to the core of the panel until shearing stresses (which can be amplified by local stress concentration) at this interface exceed the critical value and delamination initiates.
5. The ultimate strength of the core-face interface is unknown and is calculated from the experimentally-determined failure load.
6. Finally, the average shear stress at failure and/or the ultimate shear flow at critical coreface interface is calculated as:

$$\tau = \frac{VQ}{bI} \qquad \text{(Eqn. 4.8)}$$

$$q_{ult} = \frac{V_{ult}Q}{I} \qquad \text{(Eqn 4.9)}$$

where
- Q … static moment of the section above the failure plane
- I … moment of inertia of the section
- V_{ult} … ultimate shear force
- V … shear force
- b … width of the section at the critical plane (sum of thicknesses of all flats and flutes)
- τ … shearing stress
- q_{ult} … ultimate shear flow per section width

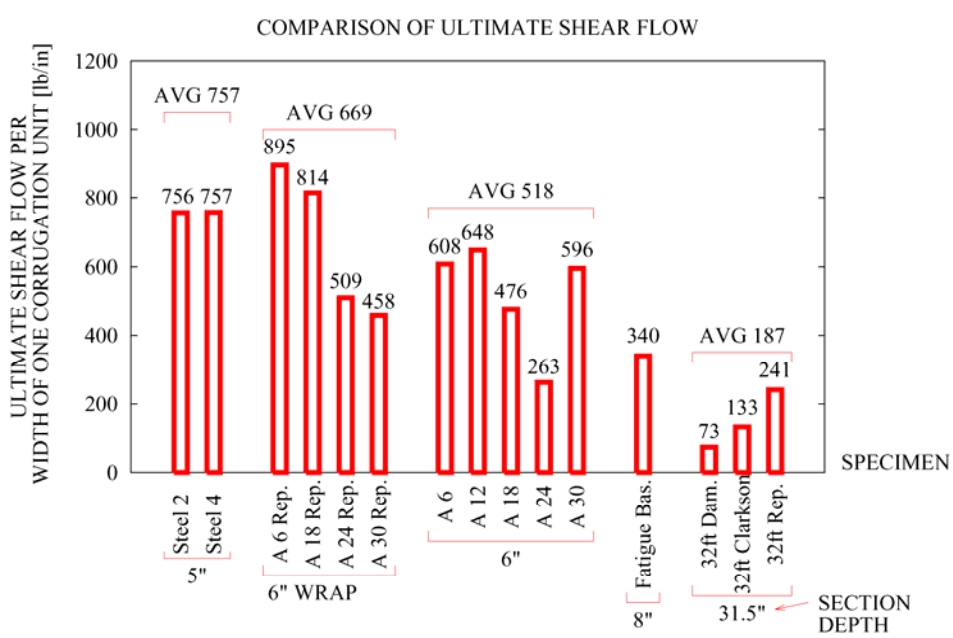

Figure 4.6: Ultimate Shear Flow for All Tested Flexural Specimens

A sample calculation of ultimate shear flow (q_{ult}) for specimen *A24 Repaired* follows:

- ultimate load (F_{ult}) = 75,260 lb → ultimate shear force (V_{ult}) = 37,630 lb (see Table 3.6)
- static moment of cross-section above failure plane (Q) = 121.14 in^3 (see Table 4.2)
- moment of inertia of the cross-section (I) = 746 in^4 (see Table 4.2)
- ultimate shear flow per width of the panel (see Equation 4.9):

$$q_{ult} = \frac{V_{ult} Q}{I} = \frac{(37{,}630\,lb)(121.14\,in^3)}{(746\,in^4)} = 6{,}110.6\,(lb/in)$$

- number of corrugation units per width = 12
- ultimate shear flow per width of one corrugation unit:

$$\frac{q_{ult}}{12} = 509.21\,(lb/in)$$

The ultimate shear flow q_{ult} is the ultimate longitudinal force per total width and unit length of the beam that must be transferred from face to the core (this shear flow is balancing the normal stresses in the face in order for the face to maintain equilibrium in the horizontal direction). To compare specimens of different widths, the total shear flow was normalized by dividing it by the number of corrugation units per panel width. Figure 4.6 shows the normalized shear flow for all specimens tested in this study. From this Figure, the following observations are made:

1. The ultimate shear flow generally decreases with increasing panel depth. This phenomenon may be explained by realizing that the moment carried by the section can be decomposed into a pair of tension and compression forces located at the centroid of the bottom and top faces, respectively. If two beams have the same span length but different depths, then for a given applied load, the deeper panel will have less shear at the core-face interface (since the moment decomposes into pair of smaller forces acting at a larger lever arm). In order to achieve same shear stresses at the interface, the applied load must be higher for deeper beams. This can result in higher localized stress concentration in the area and vicinity of the loading points and supports, which would tend to initiate a global horizontal shear failure at lower shear stress level. This local initiation (due to core buckling) was noted for the *32-ft Repaired Beam* (refer to Figure 4.5(b)). Failure of the *32-ft Repaired Beam* could have been also influenced by geometric instability, since the beam had width-to-depth ratio equal to 0.375.
2. There is a large variance in the ultimate shear flow even for members with the same face thickness and core depth (*Series A*).
3. The presence of an externally-bonded wrap increased the ultimate horizontal shear capacity for most repaired specimens. This statement can be supported by the following observations: (a) The average ultimate shear flow is generally higher for the repaired (wrapped) specimens of *Series A* than for the original (unwrapped) specimens of *Series A*. (b) The ultimate shear flow nearly doubled for the *32-ft-long Repaired Beam*. (c) Wrapped *Steel Reinforced* specimens have

values above average. Since only 2 layers of 3.0 oz ChopSM were applied as wrap for these specimens and the failure resulted in wrap rupture, it is likely that the ultimate shear flow would be even higher if more layers of 3.0 oz ChopSM were used for wrap (3 layers were used for repaired specimens of *Series A*.)

To date, efforts to determine a reliable ultimate failure criterion have only been partially successful. The complexity of the problem arises from the fact that sandwich structures generally fail by a series of local failures at internal stress concentrations (e.g. at loading points or defects), which can lead to global failure of the structure and must be accounted for. The importance of these localized failures seems to be larger for deeper sections, where the thickness of constituent laminates is smaller relative to overall panel dimensions and the stability of the core laminates may be more easily compromised.

In addition, the quality of the manufacturing process has a great impact on the ultimate carrying capacity. See general comments about *Series A* in Sec. 3.1 and more specific comments about specimen *A24* towards the end of Sec. 3.2.2.

4.3 External Wrap and Shear Friction

The presence of external wraps served to: (1) increase the ultimate strength of panels and (2) possibly reduce the variation in ultimate shear flow.

The contribution of wraps may be understood by considering a shear-friction model. Shear friction is a well-documented design procedure in structural engineering, particularly in the area of concrete and prestressed concrete structures. The shear friction concept assumes that, upon formation of a crack, it is still possible to carry shear forces across the crack by friction. The available frictional forces are equal to the product of the coefficient of friction, μ, for the crack surface and the normal force acting across the crack. For concrete structures ACI

[ACI 1999] recommends values for μ ranging from 0.45 (all lightweight concrete placed against hardened concrete not intentionally roughened) to 1.40 (normal weight concrete placed monolithically).

The normal force across the crack is provided by the reinforcement that bridges the crack. Shear-friction presumes that any crack which forms will have a rough or jagged surface, such that sliding (shear deformation) along the crack is not possible unless a perpendicular separation between the crack surfaces also occurs. It is this separation that produces the strain and corresponding force in the reinforcement.

The authors have noted that for FRPH panels there is a considerable amount of mechanical interlocking that takes place between the face laminates and core due to the manufacturing process. This mechanical interlocking is ensured when a pre-assembled core is pressed into the wet face laminate. Figure 4.7 shows the underside of a face laminate after loading and failure by horizontal shear. From this Figure, it is clear that the deformations of the face were not sheared off during the failure, and that the horizontal failure must have been accompanied by a vertical separation between the core and face laminate. Therefore, the authors believe that a similar shear-friction design concept for FRPH panels is plausible.

Figure 4.7: Photos Showing Deformations in the Face Laminate of a FRPH panel

The external wrap in FRPH panels thus performs in a similar manner to the shear reinforcement of concrete members by steel rebar. However, the failure behavior is complicated by the fact that the wrap can fail either by reaching its ultimate tensile capacity [tensile failure, see Figure 4.5(b)] or by delamination from the face [bond failure, see Figure 4.5(c)]. Wrap failures in tension are much more preferable, since the force in the wrap for design can be taken as the ultimate tensile capacity of the wrap. Wrap failures by delamination (bond failures) are undesirable from a design standpoint due to the larger scatter in resin bond properties (refer to Section 3.1). In other words, forcing the ultimate failure from the bond material to fibers, will play an important role in overcoming the obstacle of formulating reliable failure criterion.

In addition to structural enhancement, wrapping the panel can prevent moisture and surface water from penetrating into the panel and degrading the resin bonds. Therefore the external wraps serve also as environmental protection.

4.3.1 Preliminary Recommendations for Wrap Design

The purpose of this section is to develop a methodology to design wraps for FRPH panel such that most of the flange material is well utilized. This method attempts to force the ultimate failure into the wrap, as opposed to the resin failing in bond between the core and faces. The suggested design sequence is composed of the following steps:

1. For an FRPH panel section that has been transformed into the core ChopSM material, the stress in the extreme tension (bottom) fiber[19] can be expressed as:

$$\sigma_{\max} = \frac{M}{I}(h - y_c) \qquad \text{(Eqn. 4.10)}$$

where M … moment applied to the section
I … moment of inertia of the section

[19] Extreme compression (top) fiber should be considered for panels, in which buckling of the top face initiates global failure. This is likely for panels with equal thickness of top and bottom face.

h … height of the section

y_c … distance from the top of the section to the center of gravity

Assuming a linear stress-strain relationship, Eqn. 4.10 can be rewritten in the terms of strain:

$$\varepsilon_{\max} = \frac{M}{E_{core} I}(h - y_c) \qquad \text{(Eqn. 4.11)}$$

Since the purpose is to utilize the material to its maximum performance, ε_{ult} can be substituted for ε_{max} in Equation 4.11 and the ultimate moment M that the section can carry can be calculated; ε_{ult} can be obtained from the coupon test results for face laminate with 0° fiber orientation (available from Table 2.3). This base ε_{ult} can be further adjusted for different panel depths using test results presented in Chapter 3. Next, the moment can be decomposed into the pair of tension and compression forces[20] (F) acting at a lever arm *r*, which is the distance between the centroids of top and bottom faces. This leads to the following expression:

$$M = \frac{\varepsilon_{\max} E_{core} I}{h - y_c}$$

$$F \times r = \frac{\varepsilon_{\max} E_{core} I}{h - y_c}$$

$$F = \frac{\varepsilon_{\max} E_{core} I}{(h - y_c) r}$$

2. Now let's consider only the top face (the bottom face would be similar) and refer to Figure 4.8. Imposing equilibrium in the x direction on the top face of the beam between points S and T leads to the following equations for the resultant shear flow force F_{shear} acting on the top face[21]:

[20] This is based on assumption that majority of the moment is carried by the faces.

[21] Sign convention is such that forces are positive in the direction of arrows in the Figure 4.8.

$$F(s) = F_{shear} + F(t)$$

$$F_{shear} = F(s) - F(t) \qquad \text{(Eqn. 4.12)}$$

$$F_{shear} = \frac{1}{r}\left(M(s) - M(t)\right) \qquad \text{(Eqn. 4.13)}$$

3. The shear flow, *q*, can be expressed either using F_{shear} from Equation 4.13 as

$$q = \frac{F_{shear}}{\Delta x} \qquad \text{(Eqn. 4.14)}$$

or directly from the formula for the shear flow q = (VQ)/I (see Equation 4.9). The second expression provides an exact shear flow on the interface of idealized section, while the first formula provides a conservative (upper bound) estimate, since the contribution of the core to the flexural stiffness is neglected. Another advantage of the first expression for the shear flow is that it can quickly provide the total shear force (between web and core) transferred between any two points along the beam using Equation 4.12.

4. The ultimate shear flow based on ε_{max}, derived in previous paragraphs, can be used directly for the determination of wrap thickness. Design of the wrap thickness is based on the shear friction phenomena. Providing that the core-face interface has delaminated due to excessive horizontal shear forces and that the wrap now serves to prevent vertical separation between the web and faces along this interface, it follows that the wrap will be in tension. Since the interface has delaminated, the total shear flow along this interface is developed by friction and is equal to the product of coefficient of friction, μ, and the tensile force in the wrap. The force in the wrap is equal to the stress in the wrap multiplied by the total thickness of the wrap bridging critical interface. Assuming the wrap material is well anchored and cannot fail by bond, the maximum force in the wrap will occur when the wrap material reaches its ultimate tensile strength. This leads to the design expression for total wrap thickness (refer to Figure 4.9):

$$t_{wrap} = \frac{q_{ult}}{\mu \sigma_{ult}} \qquad \text{(Eqn. 4.15)}$$

where t_{wrap} … desired thickness of the wrap

q_{ult} … ultimate shear flow along the face-core interface

μ … coefficient of friction between face and core

σ_{ult} … tensile strength of the wrap

The coefficient of friction, μ, must be determined experimentally or can be roughly estimated to lie between 0.45 (conservative estimate) and 1.4. In order to determine the μ corresponding to the core-face interface of FRPH sandwich panels, double shear blocks (refer to Sec. 3.5) were manufactured for testing.

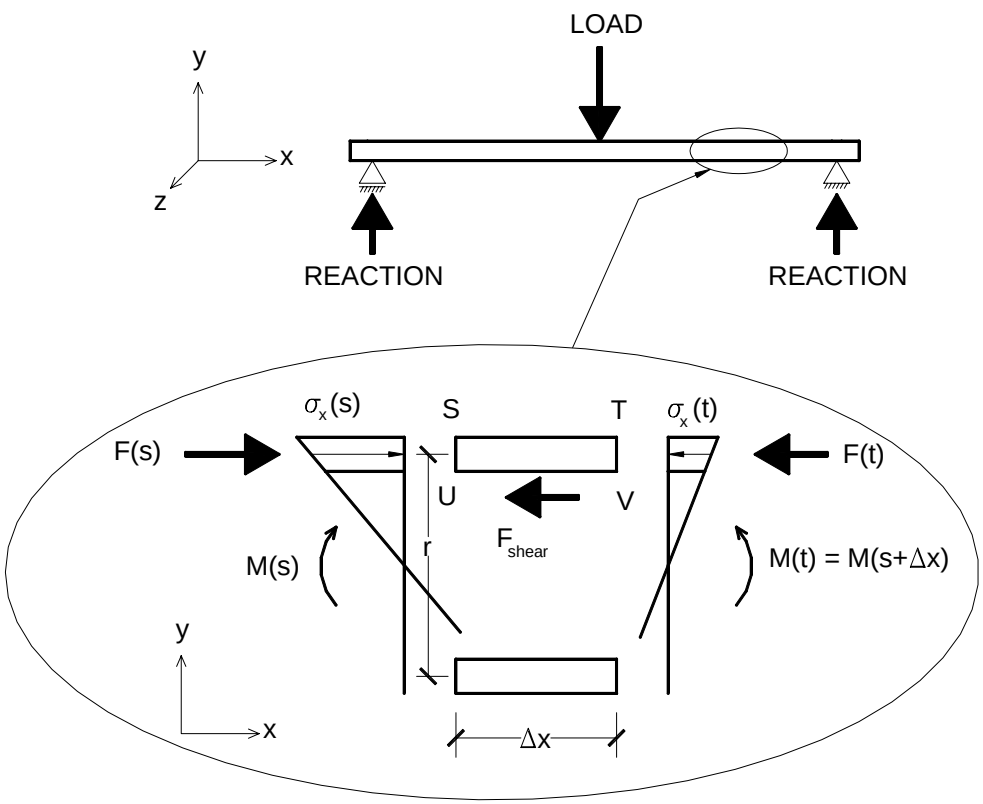

Figure 4.8: Drawing Illustrating Wrap Design (I.)

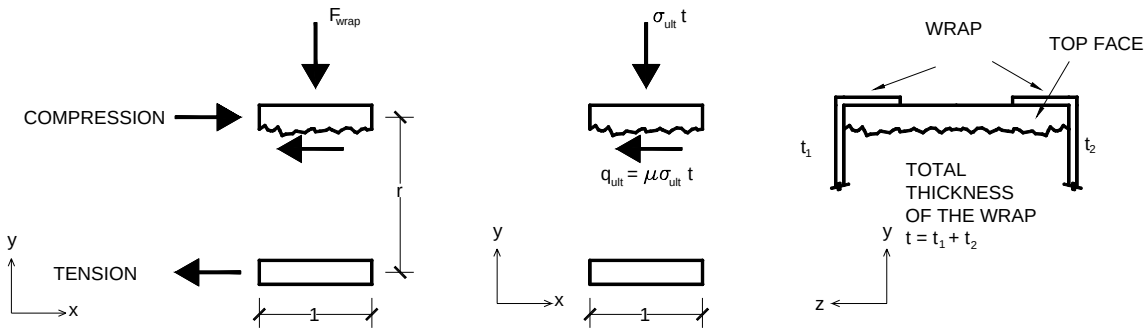

Figure 4.9: Drawing Illustrating Wrap Design (II.)

5. To ensure that the wrap is activated to its full capacity, it is important that the wrap is properly anchored. Proper anchorage forces the wrap to fail in tension, and will lead to more consistent results. Otherwise, delamination of the wrap from the faces can occur (refer to Fig. 4.5(c)) which complicates the design, since delamination is rather erratic in nature and thus very difficult to predict. Since the main concept behind the use of wraps is to shift failures from the resin to the fibers, wrap delamination is unacceptable, since it is again the consequence of resin failure.

   Proper wrap anchorage is necessary. Anchorage requirements should be based on shear strength of resin (see results of coupon tests on double lap shear specimens, Tab. 2.4). However, resin shear strength should be reduced due to the stress concentration at the end of the wrap, where combination of shear and tensile stresses occurs (Fig. 4.10). The reduction factor should be correlated to tests of entire panels. If the total required wrap thickness is large, it might be suitable to use internal wraps and/or ties as opposed to only 2 external corner wraps. Consequently, the anchorage length for each individual wrap would decrease and the clamping effect would be distributed more evenly along the panel. Another approach is to anchor the wrap between the face laminates.

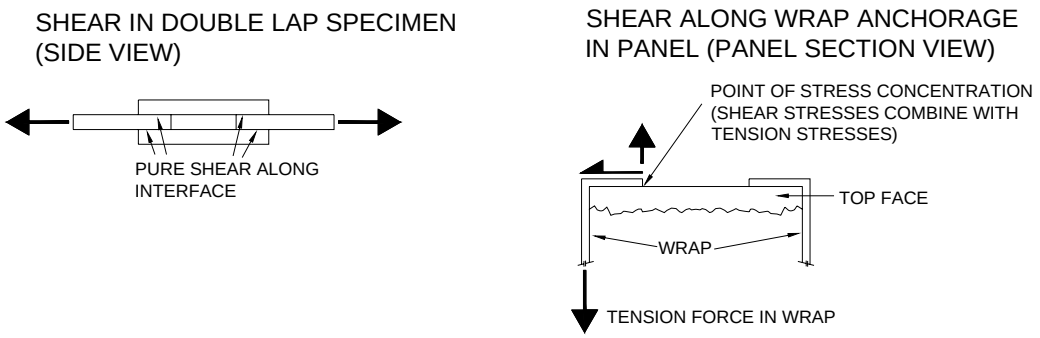

Fig 4.10: Wrap Delamination—Stress Concentration Point

4.4 FE Modeling

Several 3D Finite Element (FE) models were created using ANSYS/University High (versions 5.6.1 and 6.1) software. These models were used to asses both the overall response of the panels and to study local behaviors, including changes of stress distribution in the resin bond line due the wrap, and trends in nodal forces along the core-face interface. Analysis of overall response compared well to experimental data and is presented only briefly in this report, since it follows routine practice. On the other hand, results of local modeling are included in more detail, because they can help explain specific phenomena related to the experimental investigation.

4.4.1 Meshing

ANSYS features both free and mapped meshing. Free meshing lets the software determine the best arrangement and pattern of the elements. The user only specifies how fine or coarse the mesh needs to be. Mapped meshing allows the user to have complete control over the arrangement and pattern of the elements. Mapped meshing was used for all models for the following reasons:

1. It is easier to perform postprocessing on mapped meshes, because the user disposes the knowledge about element and node numbering. Selection of parts of the model for interpreting results can be done easily and efficiently.
2. An in-house C++ program called *MeshIt* was developed to provide tool for flexible mesh generation. By manipulating a simple input text file (see Figure 4.11), *MeshIt* can generate mapped meshes for FRPH panels with various dimensions, core geometry and mesh density. *MeshIt* generates several output files, which are directly used as macro files for ANSYS: *nodes.mac* includes a list of nodes and their coordinates, *elements.mac* holds information about elements (mainly node-element connectivity) and finally *sel.mac* serves as a macro file for flexible node and element selections.

MeshIt creates ANSYS macro files that define the geometry of the model. Material properties are specified in a separate macro file. Figure 4.12 shows an example of the mesh that was generated using the *MeshIt* routines.

```
*       Input File For MeshIt (Meshit Created By OK 2001)
*       (everything following '*' character to end of line is comment)
*       -------------
*       Series A: A-6
*       -------------

***     OPTION
        0 * (0 generate mesh template, 1 generate refined mesh)

***     SLAB PROPERTIES
*       flange coordinates (x,y,X,Y - x in longitudinal direction, y in lateral direction)
        0       0       104.63  7.06
*       core coordinates (also: x,y,X,Y)
        0.315   0.405   104.315 6.655
        5.4365   * depth of the slab
        1        * default quarterwavelength
        2.0833   * default flutewidth
        3        * number of flutes
        3        * number of flats

***     MESH PROPERTIES
*       nodes per overhang (order of directions: x,y,X,Y)
        2       2       2       2
        3        * default nodes per quarterwavelength
        11       * nodes per depth
        5        * default nodes per flutewith

***     REFINED CORE PROPERTIES (pattern specification)
*       must have (flute_# + flat_#) entries
*       so far supports: flat=0, flute_sin0=1, flute_sin90=2, flute_sin180=3, flute_sin270=4
*       type    x       y       X         width(-1)  n. per w.(-1)  1/4xL(-1)   invisible
        0       0.315   0.405   104.315   0          1             -1           0
        2       0.315   1.447   104.315  -1         -1             -1           0
        0       0.315   2.489   104.315   0          1             -1           0
        4       0.315   3.53    104.315  -1         -1             -1           0
        0       0.315   4.572   104.315   0          1             -1           0
        2       0.315   5.613   104.315  -1         -1             -1           0

***     SELECTIONS
        1 * number of selections
*       help:
*       output (generate what):
*               0 - D,no
*               1 - nsel,a,node,,no
*               2 - esel,a,elem,,no
*               3 - D,no,UX,,,,,,,UY,UZ
*               4 - D,no,UY,,,,,,,UZ
*       n0_e1 (select what): 0 - nodes; 1 - elements

*       bf0_tf1_w2 (which part): 0 - BF; 1 - TF; 2 -WEB

*       web_no (web number): starting by 0; -1 for BF and TF

*       val0_ar1 (input type): 0 - value coordinates; 1 - array coordinates

*       coord. (coordinates): x,y,X,Y
*       output  n0_e1   bf0_tf1_w2      web_no  val0_ar1        coord.
*                                               x       y       X       Y
*       2       1       1       -1      1       101     0       108     13 * load area
*
*       3       0       0       -1      1       9       0       9       14 * left support
*       3       0       0       -1      1       197     0       197     14 * right support
*
*       selections for postprocessing
*       2       1       2       0       1       0       8       206     9  * upper strips
*       2       1       2       1       1       0       8       206     9
*       2       1       2       2       1       0       8       206     9
*       2       1       2       3       1       0       8       206     9
*       2       1       2       4       1       0       8       206     9
*       2       1       2       5       1       0       8       206     9
```

Figure 4.11: Typical Input File for MeshIt

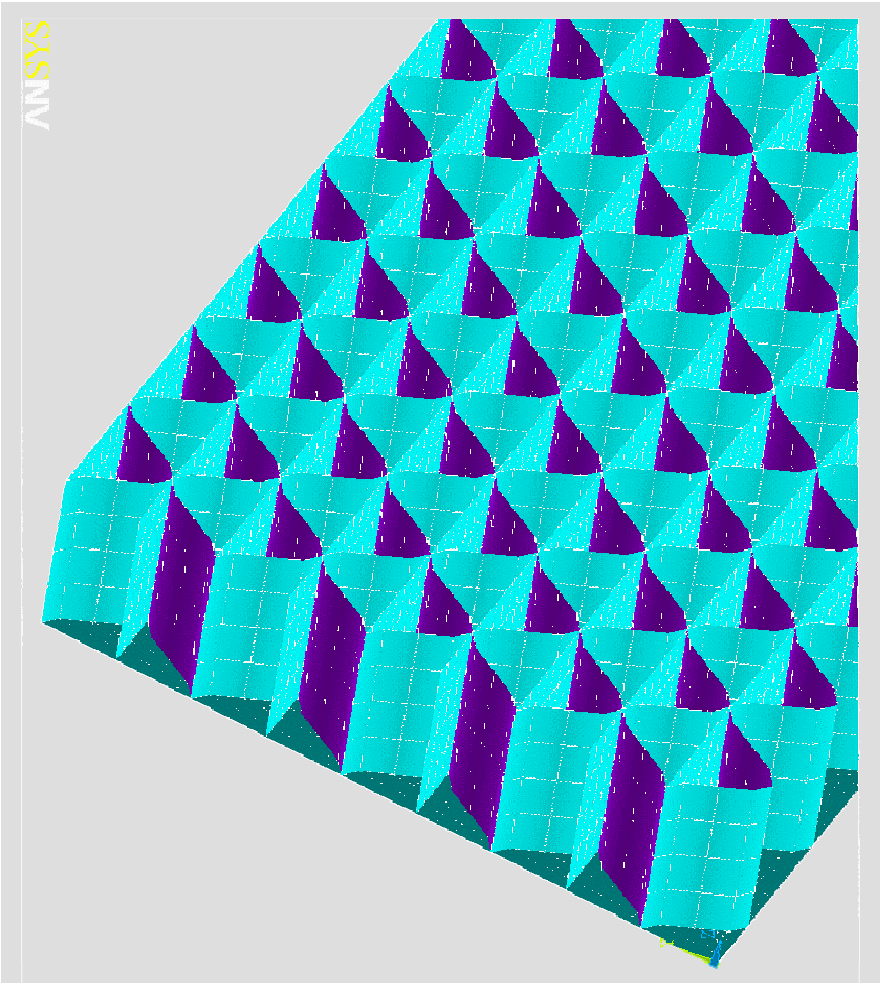

Figure 4.12: FRPH Panel Mesh in ANSYS Generated by MeshIt

4.4.2 Elements

Four-node plate elements with orthotropic material properties (refer to Tables 2.3 and 2.4) were used to model the face and core laminates. The authors is aware that this is a simplification of the real situation (e.g. extension-bending coupling is ignored) because the laminate is not simply a material, but rather a structural element for which both material properties and geometry (laminate lay-up sequence) should be taken into account [Jones 1999]. However, it is believed that this simplification can be justified because (1) the core laminate is nearly isotropic

due to the random fiber orientation and (2) the face laminate is located far enough from the neutral axis (relatively to its thickness) so the deformation of the cross-section by flexure results in an almost uniform strain distribution over the thickness of the faces. Thus, we can consider the faces as being close to only extensional loading.

4.4.3 Model 1: A6 (Overall Response)

A FE Model for specimen A6 was built to asses the ability of the model to predict overall behavior of the panel (see Figure 4.13). Comparison between experimental and theoretical deflections and strains was within 10%.

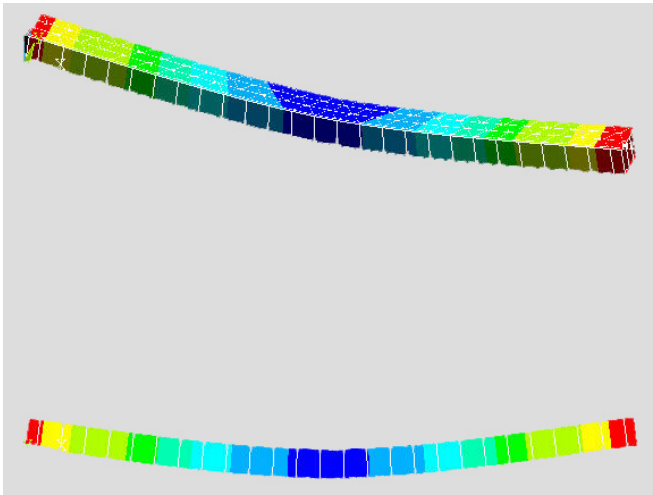

Figure 4.13: Deflection of A6 Panel Under Load in 3-pt Bending

4.4.4 Model 2: 32-ft-long Repaired Beam (Reduction of Stresses due to the External Wrap Layer)

32-ft Repaired Beam was first specimen that was tested with applied external wrap. It was also the first specimen for which FE analysis was used to investigate wrap-related phenomena.

The authors used a FE model for the *32-ft-long Beam* to asses how the wrap changed the stress distribution in the resin bond lines[22]. To accomplish this, flat ”low” elements (refer to Figure 4.14) with resin material properties were inserted between the core and top face to simulate the actual bonding condition. ANSYS analyses were then run and maximum von Mises stresses in these resin elements were recorded for each flat and flute. Von Mises stress was used because it provides a single value of stress, equivalent to the stress state at the point, and it can thus be used for direct comparison of stress levels at different location. The second step involved modeling the wrap layer. Additional elements with the wrap laminate properties were inserted over the “external resin elements.” Maximum von Mises stresses in the resin bond line were again recorded for each core wall.

Comparison of the von Mises stresses showed that a significant stress decrease due to the wrap was achieved in the external flats, while a much smaller decrease occurred in the outer most flutes. All remaining core wall interface stresses remained essentially unchanged due to the addition of the wrap (see Figure 4.15).

Results from FE modeling of the wrap suggest that any stress relief in the resin bond line is confined to the outer-most core walls. This would imply that the effectiveness of the wrap layer would be greatly diminished as panel width increases. The concept of shear friction, however, is not based on reducing stresses in the bond line but rather providing an alternate load path via frictional forces after the bond fails. Based on the shear-friction concept, the effectiveness of the wrap would depend on the relative transverse stiffness of the face laminates and seems to play an important role even for wider panels. This was demonstrated by testing

[22] This was to find whether the wrap can delay delamination by reducing stresses in the resin bond line. Delay of delamination would also delay the occurrence of shear-friction, which assumes that the wrap in not effective until delamination occurs.

Steel Reinforced and *Series A Repaired* specimens (compare ultimate shear flow in Figure 4.6 and refer to Figure 3.4).

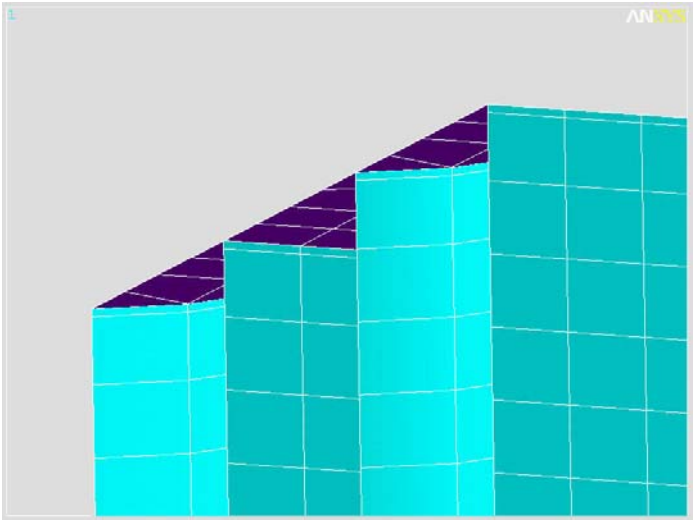

Figure 4.14: Layer of Resin Elements in ANSYS Model

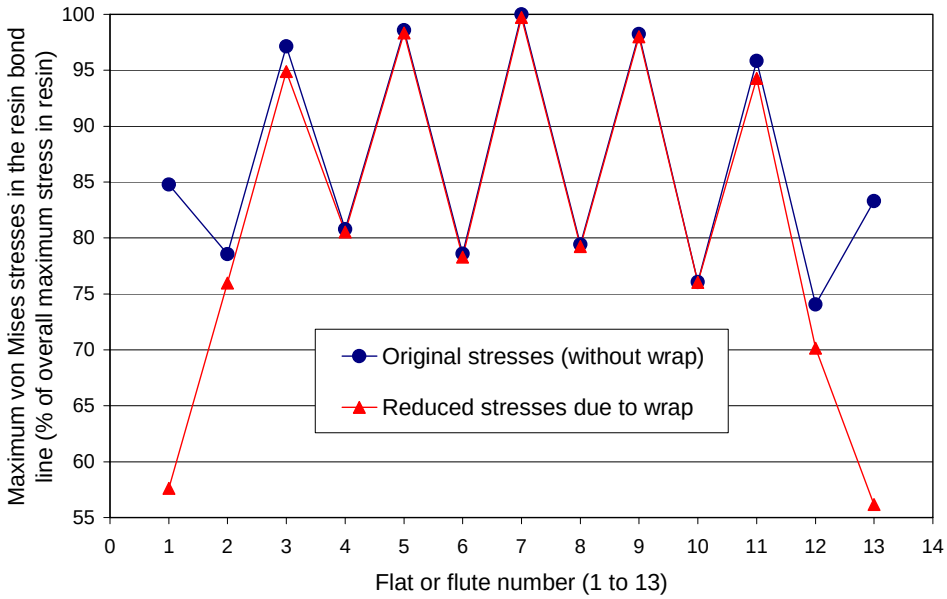

Figure 4.15: Reduction of Stresses in the Resin Interface due to the Wrap

4.4.5 Model 3: A18 (Determination of Nodal Forces Acting Along Core-Face Interface)

The purpose of performing detailed FE analysis, described in this section, was to determine the distribution of stresses between the core and faces of FRPH panel. These stresses were sought after as equivalent nodal forces in the FE model.

For the sake of simplicity, the mesh was generated for the *A18 panel* with nominal dimensions (length = 104-in, width = 180-in, total height = 6-in), refer to Figure 4.15. The width of 18-in was chosen since it would allow for a reasonable model size and yet still allow for the determination of edge-related effects. Only one half of the beam was modeled, since the panel, boundary conditions, and load were all symmetric about the "mid-span" plane (perpendicular to the longitudinal beam axis). *MeshIt* was used to generate the mesh which consisted of 25,292 nodes and 29,225 elements. The panel was loaded by uniform stresses at the contact area of a spreader beam, corresponding to the experimental ultimate load (48,880 lb). These were evenly distributed over the loading area. Imposed boundary conditions corresponded to the experimental set-up and u_x was enabled in the left support (roller), while on the symmetry plane both u_x and θ_y were fixed to zero.

Since ANSYS's ability to plot nodal loads in clear graphical form was found to be limited and difficult to perform, external software was used to visualize the desired nodal loads. In addition, the initial attempt to plot the nodal loads for one face in a single plot (as surface or contour plots) resulted in difficult-to-interpret graphs. It was therefore decided to plot nodal forces along selected flats and flutes as simple 2D graphs. Four core walls (external flat, external flute, internal flat and internal flute) were selected to study the different factors influencing nodal

force (stress) distribution. For each of the four core walls mentioned above, nodal forces F_x, F_y and F_z for both bottom and top interface were examined.

The following procedure was used:

- ANSYS allows the user to list nodal forces for selected nodes. Moreover, the user can specify (select) which elements[23] should be included in summing up the element nodal forces to obtain the resulting nodal force. In other words, the nodal force from contributing elements is a force, by which the selected elements are acting on the remaining structure (unselected elements) at the node.
- To obtain nodal forces between the bottom face and selected flats and flutes, elements of bottom face were selected first. Then, the "bottom nodes"[24] of desired core wall were selected and nodal forces listed. The same procedure was used for the top face.
- As a result of chosen procedure, the nodal forces listed in Table 4.5 and graphed in Appendix C are nodal forces acting on the core (and also represent the equivalent effect on the faces). This is important to understand the sign convention of these forces (refer to Figure 4.16).

[23] With common node.
[24] Those that are common to the core and face.

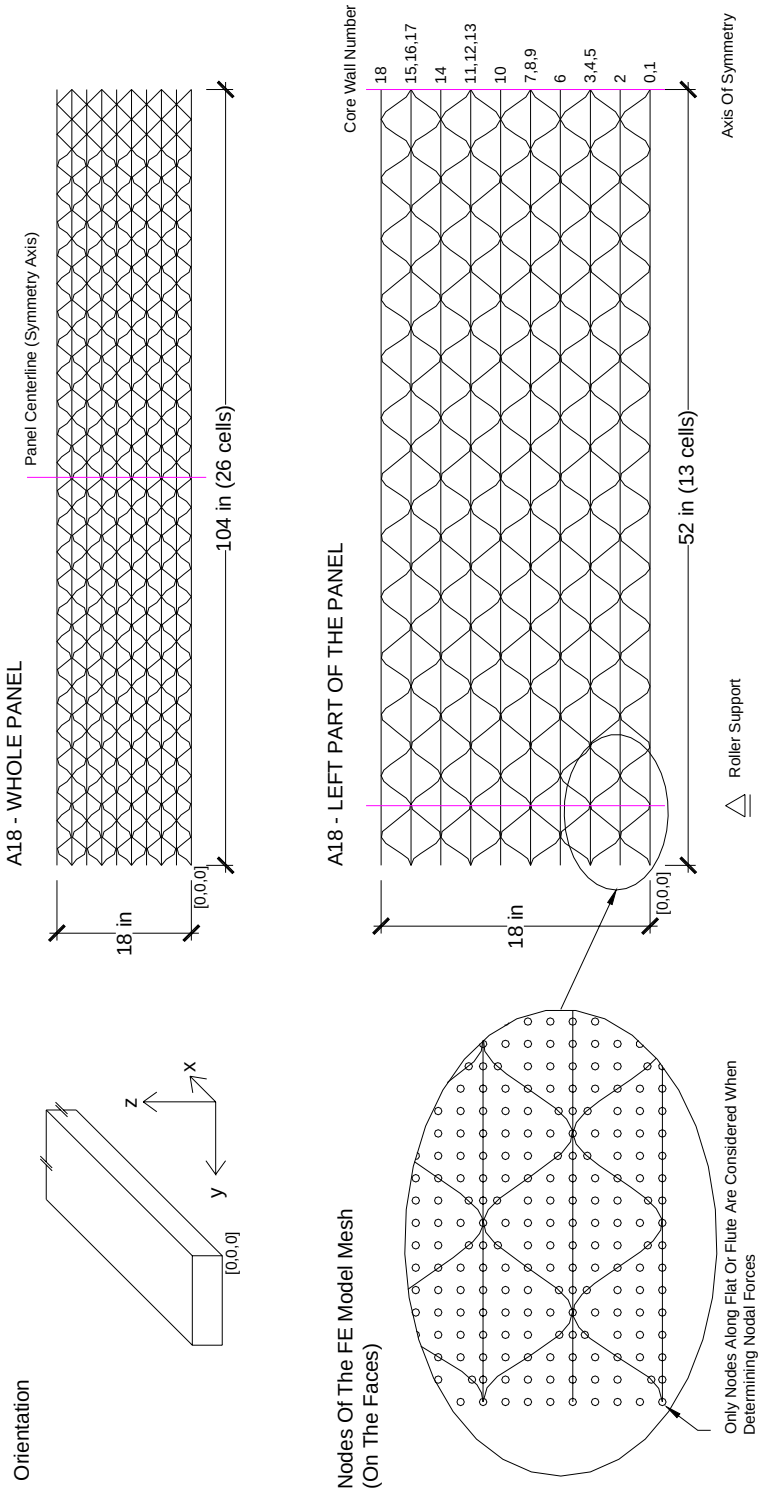

Figure 4.16: Drawing Illustrating How Nodal Forces were Extracted

Table 4.5 lists the sum of nodal forces for core walls 0, 1, 10, 11 and the whole core. At first sight, it might be a little confusing that the average based on the whole core ($F_{x,\ avg\ per\ core\ wall} \cong 174{,}500/19 = 9{,}184$ lb) is lower than any of listed values for individual flats and flutes (about 12,000 lb). However the justification is simple. This is because, if summation over individual core walls is done, some nodes (and consequently nodal forces) are accounted for more than once. When summation is done directly over the nodes of a face, each node is accounted for exactly once.

Table 4.5: Sum of Nodal Forces Along Flats, Flutes, and Core

	Top Interface			Bottom Interface		
	F_x [lb]	F_y [lb]	F_z [lb]	F_x [lb]	F_y [lb]	F_z [lb]
Web #0 (Flat)	-12,332	659	-1,531	12,701	-1,315	-633
Web #1 (Flute)	-12,417	747	15	12,397	-723	2,816
Web #10 (Flat)	-11,701	-8	-2,434	11,682	28	-506
Web #11 (Flute)	-11,979	389	-600	12,007	-587	2,109
All Flats And Flutes	-174,411	-128	-27,846	174,717	159	-337

Finally, the nodal loads[25] (F_x, F_y, F_z) for core walls 0, 1, 10, 11 are plotted in the graphs in Appendix C as function of distance from the left end of the panel, x. Based on the graphs, presented in Appendix C, the following interesting observations are made:

- Distribution of F_x along the flat core panels (Web #0 and Web #10) is quite uniform. Peaks at points for x = 8, 12, 16 … 48 are caused by the fact that contribution of adjoining flute/flutes is also accounted for at these nodes. The peaks are also constant along the length of the panel.
- Increasing peaks associated with F_y can be noted for Web #0 (Flat) but are missing for Web #10 (Flat). This could indicate stress concentrations along the edges as explained below. When the panel is loaded in flexure, the portion of the flute above the neutral axis is in compression while the portion below neutral axis

[25] It was mentioned earlier that we can imagine nodal loads as forces acting on the core and simulating the effect of faces.

is in tension. The sinusoidal shape (for flutes) deforms its geometry under uniaxial longitudinal load in addition to pure material deformation—amplitude of sinusoidal cell is getting higher for compression and smaller for tension. Consequently, if such a flute is restrained from lateral deformation (as in the core of FRPH panel), the flute in compression (top interface) "pushes outwards" while the flute in tension (bottom interface) "contracts inwards". This lateral deformation results in the transfer of lateral force (F_y) into the neighboring flats at adjoining points. The force is directly proportional to the applied moment at the section. Moreover, the force is close to zero for flats located in the center of the panel, because the effects from flutes surrounding the central flat are opposite and thus cancel each other. However, the lateral force reaches its peaks for the most external flats because the flute is free to expand outwards (compare F_y for Web #0 and Web #10). This leads to the edge stress concentration on the interface, since F_y can be up to 40% of F_x at the point (see graphs for Web #0 in Appendix C) and these two nodal force sum up in resultant shear stress.

- It is difficult to interpret the nodal forces F_z.

Chapter 5

Conclusions

Sixteen full scale FRPH panels (two *32-ft-long Beams*, three *Fatigue-Series Panels*, five *Series A-Original Panels*, four *Series A-Repaired Panels*, and two *Steel Reinforced Specimens*) were experimentally evaluated. Tests were carefully documented, with test data provided in compact form in this report, and complete test results and photographic documentation available in electronic form on the CD available from Robert Peterman (see page 3). In addition to full scale testing, two series of coupon tests and one set of shear tests on double lap shear specimens were carried out. Constituent material properties were obtained through these tests. Based on the experimental and analytical work presented in this report, the following conclusions are drawn:

- A simple procedure for stiffness determination, based on material properties from coupon tests and geometrical properties of an idealized transformed section, was found to predict deflections within 20% accuracy.
- Although two of the factors (depth of the section and use of external wrap) influencing the ultimate capacity have been identified, improving its consistency and analytical determination of failure loads is still in need of additional work. Current research suggests that using a combination of external and internal wraps or ties, in order to force the ultimate failure from the epoxy resin to the fibers, will play an important role in overcoming this obstacle. Another key factor to improve consistency in the ultimate capacity is to ensure better quality control during the manual manufacturing process. Visual inspection of the panels before and after testing revealed that several of them had severe initial defects (large pre-existing areas of delamination between the face and core), which in turn resulted in premature failure and increased the scatter in the test set.

- Outstanding fatigue performance by these panels was observed. Two specimens were subjected to 5 million cycles with a span-to-deflection (L/D) ratio of 200 (corresponding to four-times the design load), and 11 million cycles with L/D of 400, corresponding to twice the design load. Change of stiffness was insignificant during the cyclic loading. However, certain creep behavior was observed as a result of the mean fatigue load that was being applied during the duration of the test.
- The effect of width-to-depth ratio (for panels of constant depth) on unit stiffness was insignificant for the five panels tested (*Series A*). These panels had width-to-depth ratio between 1.0 and 5.0. Therefore, the ASTM recommendation [ASTM 2000] that the width of the specimen shall not be less than twice the total depth was found to be too strict for the service-load evaluation of these panels, because specimens with width-to-depth ratios smaller than 2.0 yielded the same unit stiffness properties as panels with higher width-to- depth ratio. The effect of width-to-depth ratio (for panels of constant depth) on unit strength was inconclusive, as the unit strength varied greatly between specimens with seemingly no correlation with width.
- For some full scale tests, the experimental strains in the bottom face laminate approached the failure strain of the material. This indicates a well-balanced design, as most of the material strength of the faces was utilized at ultimate loads. The material utilization can be further improved by the use of wraps that are believed to increase the minimum threshold for ultimate load and thus make the determination of ultimate load more reliable.
- The contribution of wrap was evaluated and a proposed method for wrap design was developed. However, more panels with wraps should be tested to determine the exact anchorage requirements for these wraps. This is crucial because the basic premise for the proposed formula is that the wrap will fail in tension as opposed to delamination (if the wrap delaminates, it means that anchorage requirements were not met).

- Panels with delamination damage can be successfully rebuilt, without compromising their ultimate capacity, as demonstrated by the repair and testing of the *32-ft-long Beams* and *Series A Panels*.
- Acoustic Emission monitoring was capable of detecting internal damage to the FRPH panels and should be further explored for in-situ inspection of these systems.

Chapter 6

Suggestions for Future Research

The research conducted to date established an extensive database of test data for various specimen geometries. Two major findings can be concluded: (1) The stiffness can be reasonably predicted by using either simplified or more complex design formulas or by finite element modeling. (2) The ultimate load-carrying capacity of the specimens had much greater variance then stiffness.

During the research it was found that scatter in the ultimate load-carrying capacity can be reduced by using wraps. Most of the wraps during testing, however, failed in bond and delaminated from the specimen. The next research should focus on the experimental determination of wrap anchorage, such that the wrap can achieve its full tensile capacity instead of debonding.

Once the requirements for wrap anchorage are known, the scatter in the ultimate load carrying capacity of KSCI's panels should be reduced. This will lead to an increased safety factor if the live-load deflections are limited to the current ratio of span length/800, or perhaps enable the current deflection limits to be increased.

BIBLIOGRAPHY

[AASHTO 1996] American Association of State Highway and Transportation Officials (AASHTO, 1996): *Standard Specifications for Highway Bridges.* 16th edition, Washington, D.C.

[ACI 1999] American Concrete Institute (ACI, 1999): *Building Code Requirements for Structural Concrete (318-99) and Commentary (318R-99).* Farmington Hills, Michigan 48333-9094

[Adams et al. 2000] Adams, J.S.; Ramirez, G.; Browning, J.: *Field Instrumentation and Monitoring of KDOT Fiber Composite Bridge for Long-Term Behavior Assessment*, unpublished draft of report for KDOT, [available from Robert Peterman, see page 3]

[ASTM 2000] ASTM. (2000) *Standard Test Method for Flexural Properties of Sandwich Constructions (C393-00)*, West Conshohocken, PA

[Bakis et al. 2002] Bakis, C.E.; Bank, L.C.; Brown, V.L.; Cosenza, E.; Davalos, J.F.; Lesko, J.J.; Machida, A.; Rizkalla, S.H.; and Triantafillou, T.C.: *Fiber-Reinforced Polymer Composites for Construction—State-of-the-Art Review.* Journal of Composites for Construction, Vol. 6, No. 2, May 2002

[Bank and Yin 1999] Bank, L.C., and Yin, J.: *Failure of Web-Flange Junction in Postbuckled Pultruded I-Beams.* Journal of Composites for Construction, Vol. 3, No. 4, November 1999

[Barbero 1999] Barbero, E.J. (1999): *Introduction to Composite Materials Design.* Taylor & Francis

[Data CD] Test data in electronic format are available on the Compact Disk accompanying this report

[Davalos and Qiao 1999] Davalos, J.F.; Qiao, P.: *Computational approach for analysis and optimal design of FRP beams.* Computers and Structures, v. 70, n. 2, Jan 1999, p. 169-193; Elsevier Sci Ltd, Exeter, Engl.

[Davalos et al. 2001] Davalos, J.F., Qiao, P.Z., Xu, X.F., Robinson, J., and Barth, K.E. (2001) *Modeling and characterization of fiber-reinforced plastic honeycomb sandwich panels for highway bridge applications.* Journal of Composite Structures, 52(3-4): 441-452

[Gibson and Ashby 1999] Gibson, Lorna J., Ashby, Michael F. (1999): *Cellular solids (Structure and properties)*, 2nd edition, Cambridge University Press

[Hassan 2000] Hassan, D.: *Construction of a Composite Fiber-Reinforced Polymer Bridge in the State of Kansas*, report for FWHA, available on [Data CD]

[Hayes 1998] Hayes, M.D. (1998) *Characterization and Modeling of a Fiber-Reinforced Polymeric Composite Structural Beam and Bridge Structure for Use in the Tom's Creek Bridge Rehabilitation Project.* Master's Thesis, Virginia Polytechnic Institute and State University, Blacksburg, Virginia

[Hayes et al. 2000] Hayes, M.D., Ohanehi, D., Lesko, J.J., Cousins, T.E., and Wichter D.: *Performance of Tube and Plate Fiberglass Bridge Deck.* Journal of Composites for Construction, Vol. 4, No. 2, May 2000

[Hibbeler 1995] Hibbeler, Russel C. (1995): *Structural Analysis.* 3rd edition, Prentice Hall

[Jones 1999] Jones, R.M. (1999): *Mechanics of composite materials.* 2nd edition, Taylor & Francis

[Kalny et al. 2001] Kalny, O., Peterman, R.J., and Ramirez, G.: *Performance Evaluation of a Repair Technique for Damaged FRP Honeycomb Bridge Deck Panels.* (Accepted for publication in ASCE Journal of Bridge Engineering.)

[Kalny et al. 2002] Kalny, O., Peterman R.J., Ramirez, G., Cai, C.S., and Meggers, D.: *Evaluation of Size Effect and Wrap Strengthening on Structural Performance of FRP Honeycomb Sandwich Panels.* (Presented at 2003 TRB annual meeting.)

[Lopez-Anido and Xu 2002] Lopez-Anido, R., and Xu, H.: *Structural characterization of Hybrid Reinforced Polymer-Glulam Panels for Bridge Decks.* Journal of Composites for Construction, Vol. 6, No. 6, August 2002

[NBISF 2002] National Bridge Inventory Study Foundation (NBISF). *Deficient Bridges*. http://www.nationalbridgeinventory.com/structurally deficient.htm. (Accessed Jul. 17, 2002)

[Plunkett 1997] Plunkett, J.D. (1997): *Fiber-reinforced Polymer Honeycomb Short Span Bridge for Rapid Installation.* Transportation Research Board Final Report.

[Qiao et al. 2000] Qiao, P.; Davalos, J.F.; Brown, B.: *Systematic analysis and design approach for single-span FRP deck/stringer bridges Composites.* Part B: Engineering, v31, n6-7, 2000, p. 593-609; Elsevier Science Ltd, Exeter, Engl.

[Schreiner 2000] Schreiner, J.; Barker, M.: *Lateral Distribution in Kansas DOT Steel Girder Bridge With FRP Deck*, report for Kansas State University and Kansas Department of Transportation, available on [Data CD]

[Smart Fibers Ltd: OFSSS] Smart Fibers Ltd. *Optical Fibre Strain Sensing System (OFSSS)*. http://www.opticalfibers.com (Accessed Sep. 8, 2002)

[Spears 2001] Spears, P.W.: *FRP Bridge Deck Design (KSU)*, unpublished, available on [Data CD]

[Szak et al. 1999] Szak, P.J., Bobson, B.N., Harik, I.E., and Brailsford, B.: *The Clear Creek Hybrid Composite I-Girder Pedestrian Bridge.* Journal of Composites for Construction, Vol. 3, No. 2, May 1999

[Walker and Held 1998] Walker, H.; Held, J.: *Two Years of Monitoring The First All Fiberglass Public Bridge (KSU)*, report for KDOT, available on [Data CD]

[Xu et al. 2001] Xu, X.F., Qiao, P.Z., and Davalos, J.F. (2001): *On the Transverse Shear Stiffness of Composite Honeycomb Core with General Configuration.* Journal of Engineering Mechanics, ASCE, 127(11): 1144-1151

[Zhou 1999] Zhou, G: *Development of Automated Three Dimensional Braiding Process*, Master's Thesis, Kansas State University, 1999